Energy & Environmental Science

PAPER

View Article Online
View Journal | View Issue

Cite this: *Energy Environ. Sci.*, 2016, **9**, 2418

Structural and mechanistic basis for the high activity of Fe–N–C catalysts toward oxygen reduction†

Jingkun Li,[a] Shraboni Ghoshal,[a] Wentao Liang,[b] Moulay-Tahar Sougrati,[c] Frédéric Jaouen,[c] Barr Halevi,[d] Samuel McKinney,[d] Geoff McCool,[d] Chunrong Ma,[e] Xianxia Yuan,[e] Zi-Feng Ma,[e] Sanjeev Mukerjee*[a] and Qingying Jia*[a]

Received 19th April 2016,
Accepted 10th June 2016

DOI: 10.1039/c6ee01160h

www.rsc.org/ees

The development of efficient non-platinum group metal (non-PGM) catalysts for oxygen reduction reaction (ORR) is of paramount importance for clean and sustainable energy storage and conversion devices. The major bottleneck in developing Fe–N–C materials as the leading non-PGM catalysts lies in the poor understanding of the nature of active sites and reaction mechanisms. Herein, we report a scalable metal organic framework-derived Fe–N–C catalyst with high ORR activity demonstrated in practical H_2/air fuel cells, and an unprecedented turnover frequency (TOF) in acid in rotating disk electrode. By characterizing the catalyst under both *ex situ* and *operando* conditions using combined microscopic and spectroscopic techniques, we show that the structures of active sites under *ex situ* and working conditions are drastically different. Resultantly, the active site proposed here, a non-planar ferrous Fe–N_4 moiety embedded in distorted carbon matrix characterized by a high $Fe^{2+/3+}$ redox potential, is in contrast with those proposed hitherto derived from *ex situ* characterizations. This site reversibly switches to an in-plane ferric Fe–N_4 moiety poisoned by oxygen adsorbates during the redox transition, with the population of active sites controlled by the $Fe^{2+/3+}$ redox potential. The unprecedented TOF of the active site is correlated to its near-optimal $Fe^{2+/3+}$ redox potential, and essentially originated from its favorable biomimetic dynamic nature that balances the site-blocking effect and O_2 dissociation. The porous and disordered carbon matrix of the catalyst plays pivotal roles for its measured high ORR activity by hosting high population of reactant-accessible active sites.

Broader context

Oxygen reduction reaction (ORR) constitutes a critical element in the commercialization of electrochemical energy conversion and storage devices. Consequently, the replacement of unsustainable noble metal catalysts with earth-abundant materials constitutes a vital technological strategy towards fixing the twin challenge of energy security and climate change. The success in this regard requires the development of scalable non-precious metal catalysts with high performance in practical devices, and proper understanding of the nature of active sites and reaction kinetics. In this work we developed a scalable Fe–N–C catalyst with high ORR activity demonstrated in practical H_2/air fuel cells, as well as an unprecedented turnover frequency in acid, measured with a rotating disk electrode. Combined *ex situ* and *in situ* characterizations identify a non-planar ferrous Fe–N_4 moiety embedded in distorted carbon matrix characterized by a high $Fe^{2+/3+}$ redox potential as the active site, and verify the redox mechanism. Such insights form a critical step in our ability to design and scale up future ORR catalysts.

[a] *Department of Chemistry and Chemical Biology, Northeastern University, Boston, Massachusetts, 02115, USA. E-mail: s.mukerjee@neu.edu, Q.jia@neu.edu*
[b] *Department of Biology, Northeastern University, Boston, Massachusetts, 02115, USA*
[c] *Institut Charles Gerhardt Montpellier, UMR CNRS 5253, Université Montpellier, Agrégats, Interfaces et Matériaux pour l'Energie, Montpellier, 34095, France*
[d] *Pajarito Powder, LLC (PPC), Albuquerque, New Mexico 87102, USA*
[e] *Shanghai Electrochemical Energy Devices Research Center, Department of Chemical Engineering, Shanghai Jiao Tong University, Shanghai 200240, People's Republic of China*

† Electronic supplementary information (ESI) available: Additional information including the EXAFS and XANES analysis, effective electrochemical surface area calculations, turnover frequency calculations, BET surface area summary, H_2/air PEMFC performance with the scale-up catalyst, and the RDE testing results. See DOI: 10.1039/c6ee01160h

1. Introduction

Eliminating noble metals such as those of the platinum group (PGM) for cathodic oxygen reduction especially at the interface with polymer membranes provides for market transformation of several key technologies ranging from energy conversion in fuel cells to energy storage devices.[1,2] The rapid escalation of catalytic activity of non-platinum group metal (non-PGM) catalysts reported recently has shown great promise for M–N–C materials (M = Fe and/or Co).[3,4] M–N–C materials synthesized through pyrolysis of precursors comprising of transition metals, nitrogen, and carbon at high temperatures (700–1100 °C)

constitute the leading non-PGM candidates for the oxygen reduction reaction (ORR) thus far.[5–9] In view of the present trial-and-error approach optimizing performances *via* tuning the synthetic routes and precursor materials, further improvements relies heavily on proper understanding of the nature of active sites and their catalytic roles toward ORR.

Significant efforts have been devoted to elucidating the active sites in M–N–C catalysts.[5,10–18] To date, three types of active sites have been shown to exhibit decent ORR activity in acidic media: metal–nitrogen moieties embedded in carbon (denoted as MN_xC_y),[9,11,14,16,18,19] nitrogen–carbon moieties (denoted as N_xC_y),[20,21] and nitrogen doped carbon encapsulating inorganic metal species (denoted as $M@N_xC_y$).[6,22,23] The major difference within the three types of active sites lies in the role of the transition metal M. As for MN_xC_y moieties, it is widely believed that the metal M constitutes the core of the active site,[11,18,19,24,25] and the high turnover frequency (TOF) of MN_xC_y moieties is controlled by a moderate M–O binding energy.[14,16,26] Contrarily, others argue that the transition metal only serves to catalyze the formation of N_xC_y active sites during the pyrolysis rather than being part of the active sites, and the ORR activity is exclusively attributed to metal-free N_xC_y sites.[27,28] While it is debatable whether N–C materials prepared with precursors containing M are really "metal-free" given that even trace amount of MN_xC_y moieties can significantly boost the ORR activity of M–N–C materials,[21,29] unadulterated N–C materials do show some ORR activity in acidic media.[20,30] Guo *et al.*[20] recently showed that the active sites of N–C materials are the carbon atoms next to pyridinic N with Lewis basicity. These may also be the active sites of $M@N_xC_y$ species, for which the encapsulated M does not participate in the ORR directly but facilitates the ORR *via* favorable modification of the electronic properties of the carbon matrix.[6,23]

While a consensus has been reached that all three types of active sites are to different extents catalytically active toward ORR in acidic conditions, the relative contributions of each type of site to the overall ORR activity of pyrolyzed M–N–C materials is still a controversial subject. This is mainly because all three types of active sites co-exist in most of the pyrolyzed M–N–C materials, rendering difficult correlations between the overall measured activity and the iron speciation. Given that N_xC_y sites are always present in pyrolyzed M–N–C materials, numerous efforts have attempted to separately evaluate the specific activity and selectivity of $M@N_xC_y$ and MN_xC_y species.[5,6,31] Most recently, Fe–N–C catalysts without any $Fe@N_xC_y$ species were successfully developed and exhibited exceptional ORR activities and near $4e^-$ pathway in acidic media.[5,31] The authors accordingly inferred that the $Fe@N_xC_y$ species made insignificant contributions to the overall ORR activity in acid electrolyte relative to the contribution from co-existing FeN_xC_y moieties. This is in line with Dodelet's study that shows the ORR activity of the state-of-the-art Fe–N–C catalysts containing FeN_xC_y moieties are usually much higher than those of Fe–N–C catalysts containing only inorganic Fe species.[32] However, a metal organic framework (MOF)-derived Fe–N–C catalyst free of any FeN_xC_y species was recently developed, having an ORR activity comparable to state-of-the-art Fe–N–C contemporaries in acidic media.[6] This can be explained as the reactivity of $M@N_xC_y$ species varies with the thickness of the N-doped carbon shells surrounding the metal core.[33,34] This thickness may depend from the different preparation routes and/or using different precursors. Despite the uncertainty of $M@N_xC_y$ species' catalytic roles, high ORR activity is demonstrated on Fe–N–C catalysts that do not contain any $Fe@N_xC_y$ species. The ORR activity is mostly attributed to FeN_xC_y moieties rather than N_xC_y sites since the ORR activities of N_xC_y sites are generally significantly inferior, at least in acidic media, to their FeN_xC_y counterpart sites.[29,35] Alternatively, some researchers believe that both FeN_xC_y moieties and N_xC_y sites are required to efficiently perform the 4 electron ORR on the basis of dual site mechanisms.[15,36]

Although ample experimental[5,14,17,18,31,35] and computational[14,37–39] evidence reported thus far point to the pivotal roles of FeN_xC_y moieties for the ORR activity of pyrolyzed Fe–N–C catalysts, the exact structures of the FeN_xC_y moieties formed upon high temperature pyrolysis are still under extensive debate, and how these sites mediate the ORR in electrochemical conditions also remains elusive, with little *operando* spectroscopic data being available hitherto. There appears to be a growing consensus that at least two types of $Fe–N_4$ moieties coexist, namely a ferrous low-spin $Fe–N_4$ site (D1) and a ferrous intermediate spin $Fe–N_4$ site (D2),[5,11,17,18,31,40] and that D1 is mainly responsible for the ORR activity.[11,12,17,31] The high intrinsic ORR activity of D1 is ascribed to the high electron density at the central Fe ion.[12] It is noted that these results are drawn largely on the basis of *ex situ* Mössbauer spectroscopy characterizations. Different results have been reported based on other techniques. Most recently, Zitolo *et al.*[5] argued that the two $Fe–N_4$ moieties shall be assigned to in-plane or near in-plane $Fe–N_4$ porphyrinic architectures with two different O_2 adsorption configurations (the central Fe is hexa- or penta-coordinated with 5th and/or 6th axial oxygen ligand), and the site is formed *via* integration of $Fe–N_4$ moieties at the bridging edges of graphitic pores or zigzag graphene edges, based on *ex situ* X-ray absorption spectroscopy (XAS) analysis. Moreover, they stated that the high ORR activity of the sites is not solely determined by the local geometry of the active sites but is also positively tuned by the basicity of the N-doped carbon matrix, which was also shown to be critical for the ORR activity of N_xC_y sites recently.[20] In parallel, by employing *in situ* XAS, we recently confirmed the $Fe–N_4$ local configuration of Fe-sites in macrocycle-derived and polymer-derived Fe–N–C materials. However, the central Fe cation was found to be out-of-plane under reducing electrochemical conditions.[14,16] Moreover, we demonstrated that the central Fe moves back in the N_4-plane at high potential, following oxidation state change and adsorption of oxygen adsorbates. This behavior is opposite to that observed with non-pyrolyzed $Fe–N_4$ macrocycles.[14] This unusual in-plane/out of plane switching behavior accounts for the superior ORR activity of pyrolyzed Fe–N–C materials by optimizing the bond strength between the Fe center and the ORR intermediates. Overall, these recent advances using *in situ* synchrotron-based X-ray spectroscopy techniques appear to highlight the complexity of such materials. It is unclear whether these discrepancies are induced by the different

structures of active sites between *ex situ* and *in situ* conditions, or by the bias caused by the inherent limitations of different techniques, or both. The verifications of these questions will greatly advance the fundamental understanding of the nature of active sites in M–N–C materials.

In this work, a highly active MOF-derived Fe–N–C catalyst with a majority of Fe as FeN_xC_y moieties and a minimum amount as $Fe@N_xC_y$ sites is developed using a facile and scalable method. A variety of microscopic and spectroscopic techniques including *ex situ* Mössbauer and *in situ* XAS are combined to elucidate the structural and mechanistic basis of the high performance of this catalyst. In particular, detailed comparison analysis between *ex situ* XAS and Mössbauer results, and between *ex situ* and *in situ* XAS is conducted to address the discrepancies regarding the nature of active sites. We show that the discrepancies can be addressed by assigning the D1 site to an in-plane high-spin Fe^{3+}–N_4 moiety rather than a low-spin Fe^{2+}–N_4 moiety previously proposed based on *ex situ* characterizations. The local configuration of D1 under *ex situ* conditions cannot be directly linked to the measured activity as it is identical to the configuration identified at elevated potentials when the site is ORR inactive with the central Fe cation poisoned by oxygen adsorbates. The local configuration switches to an out-of-plane Fe^{2+}–N_4 configuration when the potential is decreased below the $Fe^{2+/3+}$ redox potential. The close correlation between the $Fe^{2+/3+}$ redox potential and the onset of ORR observed electrochemically is rationalized by the findings that the number of available active sites decreases sharply when the applied potential crossing the redox potential anodically. This verifies that the site-blocking effect governed by the $Fe^{2+/3+}$ redox potential plays a dominant role for the catalytic activity of FeN_xC_y sites. A comprehensive understanding of the unprecedented TOF value of the active site in this catalyst is given on the basis of the established redox mechanism.

2. Results

2.1 Physicochemical characterizations

The FePhenMOF–$ArNH_3$ catalyst is synthesized by mixing the metal organic framework (MOF) template formed *via* the reactive ball milling with Fe and N precursors, followed by two heat treatments, first in Ar and then in NH_3, respectively (Fig. 1). Multiple techniques are combined to characterize the MOF-derived material at different synthesis stages to track the formation of the final products. The powder X-ray diffraction

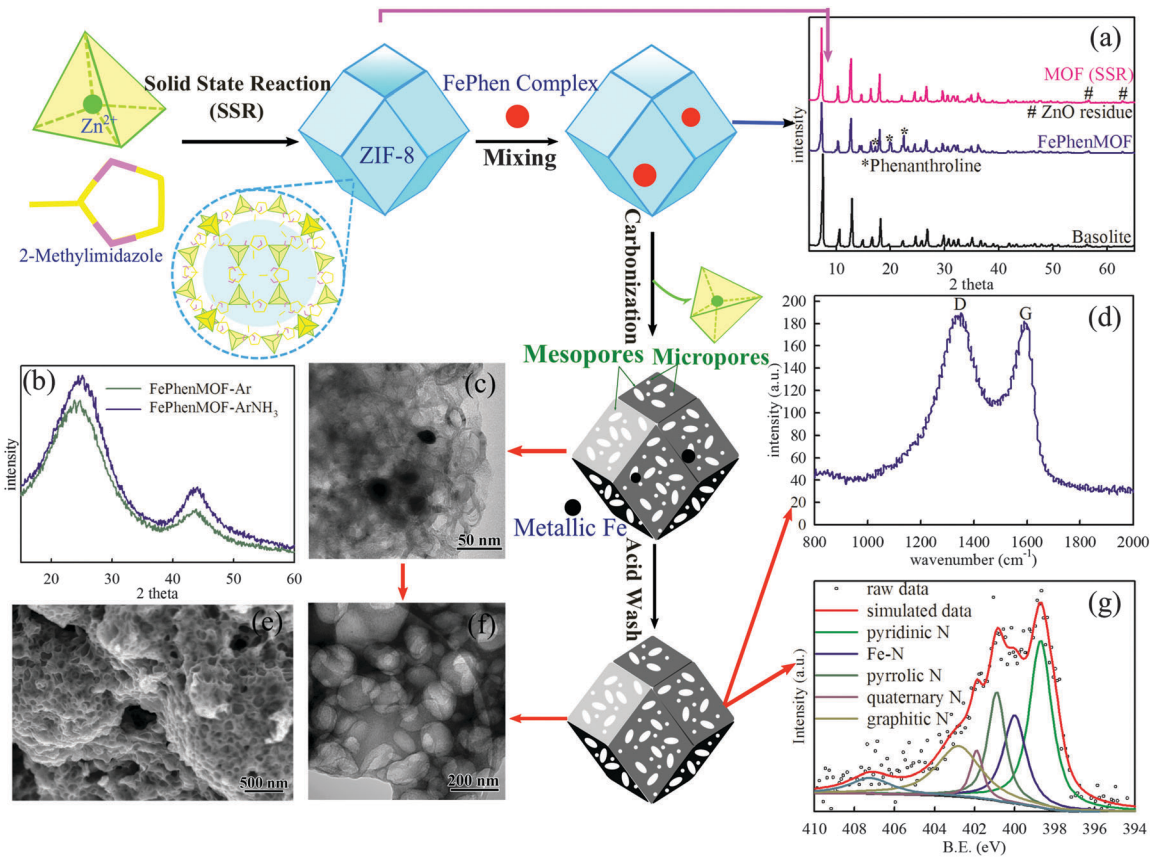

Fig. 1 Schematic illustration of the synthesis procedure of the FePhenMOF–$ArNH_3$ catalyst and the physicochemical characterizations. (a) X-ray diffraction pattern of non-pyrolyzed MOF, FePhenMOF and Basolite Z1200®. (b) X-ray diffraction pattern of FePhenMOF–Ar and FePhenMOF–$ArNH_3$. (c) TEM image of FePhenMOF–$ArNH_3$ before acid wash; scale bar, 50 nm. (d) Raman spectrum of FePhenMOF–$ArNH_3$ after acid wash. (e) SEM image of FePhenMOF–$ArNH_3$; scale bar, 500 nm (f) TEM image of FePhenMOF–$ArNH_3$ after acid wash; scale bar, 200 nm. (g) XPS spectra of N 1s for FePhenMOF–$ArNH_3$.

(XRD) spectra of the MOF synthesized through a solid state reaction, in comparison with the as-received Basolite® (Sigma, Basolite Z1200) confirm the formation of the crystalline ZIF-8 structure (Fig. 1a). This structure remains undisturbed upon ball milling of the mixture of the as-prepared MOF and iron(II) acetate and 1,10-phenanthroline, though extra peaks from the phenanthroline are observed in the product FePhenMOF (Fig. 1a). This suggests the presence of free 1,10-phenanthroline in the near-surface region rather than in the inner body, otherwise a positive shift in XRD peaks caused by encapsulation of phenanthroline within the MOF would be observed, as shown in our previous work.[6] In that work, the phenanthroline and iron(II) acetate were mixed with other precursors *via* a wet chemical method during the formation of the MOF. The Fe-species in the final products are exclusively inorganic Fe species encapsulated by graphitized carbon ($Fe@N_xC_y$), which is ascribed to the effective encapsulation of phenanthroline and iron(II) acetate promoted by the synthesis route. On the other hand, in the present study the MOF had already been formed *via* the solid state reaction prior to the addition of phenanthroline and iron(II) acetate. The Fe-species including both FeN_xC_y and metallic Fe are preferentially formed in the near surface regions in a decorated manner, which is reasonably attributed to the absence of encapsulation of Fe and N precursors in this route. These comparison results clearly show that the final products in MOF-derived materials are controllable, despite their extreme sensitivity to the synthesis route.

The formed FePhenMOF precursor is subjected to pyrolysis (1050 °C) in Ar atmosphere (denoted as FePhenMOF–Ar hereafter), followed by a second pyrolysis at 1050 °C in NH_3 (denoted as FePhenMOF–$ArNH_3$ hereafter). The first pyrolysis transforms the crystalline FePhenMOF precursor into a disordered carbonaceous material as shown by the absence of sharp XRD diffraction lines, except for two broad peaks typical for amorphous carbon (Fig. 1b). The high disorder of the carbon matrix is further supported by the Raman spectra where the intensity of the D-band (disorder vibration mode) is higher than that of G-band (graphitic carbon) (Fig. 1d).[41] The amorphous MOF-derived materials also exhibit porous, alveolar, and interconnected hollow structures as clearly seen by transmission electron microscopy (TEM) (Fig. 1c), and abundant macropores (50–100 nm) displayed in the scanning electron microscopy (SEM) images (Fig. 1e). These properties have been previously observed on analogous MOF-derived materials,[5,6,8] and demonstrated to facilitate the mass transportation of ORR-related species and water towards and away from the catalytic active sites that is critical for fuel cell performance. Another advantage of the MOF is the high BET area that is closely related to active site population.[8,17,42] The second pyrolysis in NH_3 drastically increases the BET area from 378 $m^2\ g^{-1}$ to an ultra-high value of ~1360 $m^2\ g^{-1}$ (ESI,† Fig. S1). More specifically, the surface area of micropores increases drastically from 115 to 872 $m^2\ g^{-1}$ (ESI,† Table S1). This is critical for ORR activity as the micropores host most of the active sites, and a nearly linear correlation between the micropore surface area of Fe–N–C catalysts and the ORR activity has been reported.[43,44] The enhanced porosity is ascribed to the formation of pores by the etching of the carbon by NH_3, and more time and space for trapped Zn atoms to escape as volatile products.

While the high temperature (≥700 °C) pyrolysis brings on many favorable aspects of the FePhenMOF–$ArNH_3$ catalyst, it also causes the formation of agglomerated inorganic Fe species as seen by TEM (Fig. 1c), which becomes indiscernible upon acid-leaching of the catalyst (Fig. 1f). Only minimal amount of inorganic Fe species is observed by Mössbauer spectroscopy and X-ray absorption spectroscopy (XAS) as shown later in Fig. 3. These results together demonstrate that the inorganic Fe species in FePhenMOF–$ArNH_3$ is nearly completely dissolved in acid, which differs from most previously reported pyrolyzed Fe-based catalysts,[6–8,15,18] for which some inorganic Fe species encapsulated in carbon ($Fe@N_xC_y$) is stable in acid. The absence of $Fe@N_xC_y$ is likely related to the omission of the wet impregnation step during the synthesis, given that the Fe-based catalysts free of $Fe@N_xC_y$ after acid-leaching recently reported by Bogdanoff's and Kramm's[31] and Jaouen's[5] groups were also synthesized *via* a dry mixing preparation method. In addition, the complete removal of inorganic Fe species upon acid-leaching in this work supports the hypothesis that such species were selectively formed in the near-surface region, easily accessible to the acidic electrolyte. Since the catalytic role of $Fe@N_xC_y$ is unclear so far,[6,15,31] the absence of these species in FePhen-MOF–$ArNH_3$ offers good opportunity to elucidate the structure–activity correlations of FeN_xC_y moieties.

The FeN_xC_y species in the near-surface region of FePhenMOF–$ArNH_3$ was first probed by X-ray photoelectron spectroscopy (XPS). XPS confirms that the nitrogen content in FePhenMOF–$ArNH_3$ is ~6.0 wt% with varying contributions from pyridinic, Fe–N_x, pyrrolic, quaternary, and graphitic nitrogen species (Fig. 1g) (full information of the at% and wt% of C, N, O, and Fe detected by XPS are given in ESI,† Table S2). Such high concentration of nitrogen requires chemical coordination of the metal sites as directly evidenced by the relatively high Fe–N_x peak intensity (binding energy of 399.9 eV). The ultra-high content of pyridinic N (398.7 eV), which was proposed to be a descriptor for edge plane exposure since it is preferentially located at the edges of the carbon layers,[45] has been positively related to the ORR activity for metal-containing catalysts.[35] In addition, distorted FeN_xC_y species also contribute to the pyridinic nitrogen XPS peak.[35] Therefore, the high content of pyridinic N in FePhenMOF–$ArNH_3$ indicates high content of distorted FeN_xC_y species embedded in the defects and edges populated in the porous carbon matrix as corroborated by XAS shown below.

2.2 Electrochemical testing

The FePhenMOF–$ArNH_3$ catalyst was electrochemically characterized with a rotating ring disk electrode (R(R)DE) and in a practical H_2/air proton exchange membrane fuel cell (PEMFCs) (Fig. 2). It exhibits a current density of ~50 mA cm^{-2} at 0.8 V in a PEMFC (without IR corrections) and a peak power density of ~0.4 W cm^{-2} at 0.4 V (or a current density of 1 A cm^{-2}), reaching approximately 64% the power density of the Pt-cathode under the same operating conditions (Fig. 2a). The performance of the

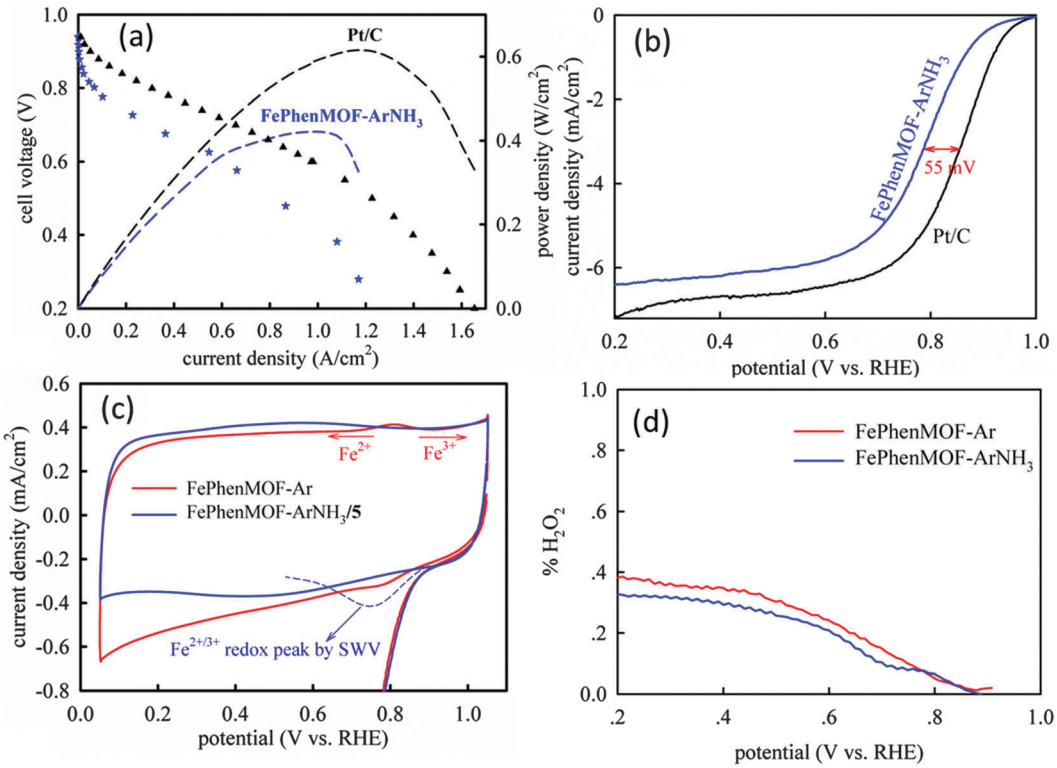

Fig. 2 (a) H_2/air fuel cell polarization curves and corresponding power density curves for same MEA collected with FePhenMOF–$ArNH_3$ (loading of 2 mg cm^{-2}), a Pt/C (0.4 mg_{Pt} cm^{-2} loading) cathode reference was used for comparison (detailed experimental information provided in the Experimental section). (b) Rotating ring disk electrode (RRDE) ORR polarization plots collected with FePhenMOF–$ArNH_3$, Tanaka Pt/C in O_2-saturated 0.1 M $HClO_4$ electrolyte at 20 mV s^{-1} with rotation rate of 1600 rpm at room temperature. (c) Cyclic voltammogram (CV) plots collected with FePhenMOF–$ArNH_3$ and FePhenMOF–Ar in Ar-saturated 0.1 M $HClO_4$ electrolyte at 20 mV s^{-1} at room temperature, together with the ORR polarization plots (cathodic scan) with rotation rate of 1600 rpm; the plots of FePhenMOF–$ArNH_3$ are divided by a factor of 5 for comparison purposes; the comparison plots without scaling are displayed in ESI,† Fig. S3. The $Fe^{2+/3+}$ redox peak of FePhenMOF–$ArNH_3$ (blue dashed line) is obtained by square-wave voltammetry. (d) Percentage of H_2O_2 released during ORR. The ring currents were collected concurrently with the disk currents shown in (c) for FePhenMOF–$ArNH_3$ and FePhenMOF–Ar.

FePhenMOF–$ArNH_3$ catalyst is among the highest activities of non-PGM cathodes reported in real PEMFCs.[5–8] In addition, the FePhenMOF–$ArNH_3$ catalyst has been successfully scaled up to 150 grams of the MOF precursor and 6 grams of the final catalyst out from the 30 grams of FePhenMOF precursor (the yield of the heat treatments is 20%, which is comparable with our lab-scale synthesis) with comparable PEMFC performance at the present stage (ESI,† Fig. S2 with detailed procedure for scale up provided).

FePhenMOF–$ArNH_3$ also exhibits exceptional ORR activity in RDE. It shows an onset potential (E_o defined as the potential with the associated current density reaching 1% of the limiting current density) of 0.98 V *vs.* reversible hydrogen electrode (RHE) (hereafter, all the potentials mentioned in this paper are *versus* RHE unless otherwise specified) and a half-wave potential ($E_{1/2}$) of ~0.78 V (Fig. 2b). This represents only ~55 mV deviation from that of commercial Pt/C (46 wt% Tanaka) despite the ultralow Fe loading (0.5 wt% as confirmed by inductively coupled plasma mass spectrometry (ICP-MS)), implicating the high intrinsic activity of active sites in this catalyst. The unprecedented TOF of the active site in this catalyst will be reported and thoroughly discussed later.

As clearly seen in Fig. 2c, the ORR onset of the catalyst is strongly correlated to the $Fe^{2+/3+}$ redox peak obtained by square-wave voltammetry (SWV). This correlation has been previously observed on various Fe–N–C catalysts, and considered as strong evidence for the direct involvement of the central Fe ion in the ORR *via* the redox mechanism.[14–16,24] This $Fe^{2+/3+}$ redox peak is indiscernible in the broad CV of FePhenMOF–$ArNH_3$, likely a result of being overwhelmed by the high double layer capacitance (Fig. 2c and ESI,† Fig. S3). Interestingly, the FePhenMOF–Ar catalyst without the subsequent pyrolysis in NH_3 exhibits a much narrower CV and a pair of well-defined $Fe^{2+/3+}$ redox peaks around 0.78 V, comparable to the redox potential of FePhenMOF–$ArNH_3$ obtained by SWV. Moreover, both the double layer capacitance and the ORR polarization curve in the kinetic region of FePhenMOF–Ar nearly overlap those of FePhenMOF–$ArNH_3$ divided by a factor of five (Fig. 2c). The effective electrochemical surface area (S_a) derived from the double layer capacitance (detailed calculations are provided in ESI†)[46,47] is close to the micropore surface area for both catalysts (ESI,† Table S1). This strongly suggests that the micropores, which by themselves are hardly accessible by electrolytes and molecules,[47,48] make significant contributions to the S_a that is primarily contributed from pores accessible by the electrolytes and molecules.[48] This is made possible by the relatively populated mesopores and macropores that effectively transport reactants and products

toward and away the active sites in micropores.[49] This indicates that while the second pyrolysis in NH_3 greatly increases the population of active sites available for ORR by increasing the population of pores accessible to the electrolyte and molecules, it does not alter the nature of the active sites. This is in line with the recent findings on analogous MOF-derived Fe–N–C catalysts that the XANES and Mössbauer spectra before and after the second pyrolysis in NH_3 are identical,[5] and multiple heat treatments enhance the utilization of active sites.[40] Therefore, the improved ORR activity induced by the second pyrolysis in NH_3 is attributable to the increased active site population accessible for ORR, and/or the higher basicity of the carbon matrix, as proposed by Zitolo *et al.*,[5] rather than assigned to a hypothetical change in the structure of the active sites. These results together strongly suggest that the redox mechanism we established on intact macrocycles, macrocycle-derived, and polymer-derived Fe–N–C catalysts[14–16] are also applicable to the MOF-derived Fe–N–C catalysts, which will be confirmed by *in situ* XAS shown below.

The low percentage of H_2O_2 released during ORR as evidenced with the measured ring current in the RRDE indicates the full $4e^-$ reduction of oxygen to water (Fig. 2d) for both catalysts. The comparable H_2O_2 yields between the two catalysts, despite their drastically different active site population, further suggests that the $4e^-$ reduction is delivered by one active site rather than two adjacent active sites through dual site mechanisms.[15,36]

To probe the structural and mechanistic basis of its high ORR activity, the FePhenMOF–$ArNH_3$ catalyst was subjected to *ex situ* Mössbauer and *in situ* XAS characterizations. Both of these spectroscopic techniques have proven extremely suitable for characterizing Fe-based catalysts as they are ultra-sensitive to the electronic configuration and coordination environment of the central Fe ions in the complex materials.[5,6,11,14–18] Furthermore, the combination of these two complementary techniques offers unique advantages in elucidating the nature of the active sites as the *in situ* XAS can quantitatively determine the bulk average bond distance, coordination number, oxidation state of the central Fe under operating conditions, while Mössbauer can distinguish between analogue Fe–N sites with different oxidation and/or spin states.

2.3 *Ex situ* characterizations

The Mössbauer spectrum of the FePhenMOF–$ArNH_3$ catalyst was fitted with two doublets, in addition to a singlet assigned to γ-Fe (Fig. 3a) representing 6.5% of the resonance area. The doublet D1 has been widely observed in both Fe-macrocycle-pyrolyzed catalysts[10–12] and Fe–N–C catalysts synthesized from individual Fe, N, and C precursors,[5,17,18] and commonly assigned to the low spin Fe^{2+}–N_4 moiety. The isomer shift (IS) and quadrupole splitting (QS) values of D2 are typical for the square-planar intermediate-spin Fe^{2+}–N_4 moiety in the ferrous iron phthalocyanine (FePc).[25,50] Bulk FePc is thus measured by XAS here to obtain a reference spectrum of D2. The shoulder at 7117 eV in the XANES (Fig. 3c), which arises from the $1s \rightarrow 4p_z$ transition with simultaneous ligand to metal charge transfer,[51]

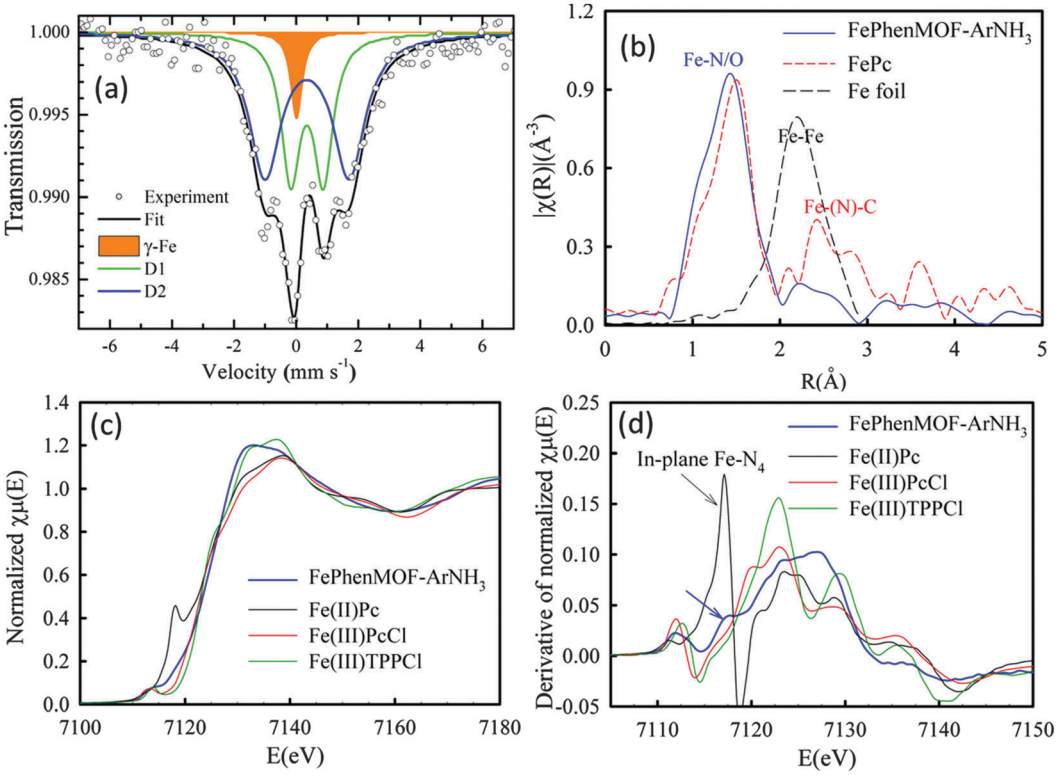

Fig. 3 Room temperature Mössbauer absorption spectrum and its deconvolution for the FePhenMOF–$ArNH_3$ dry powders (a) and the corresponding *ex situ* FT-EXAFS (b), XANES (c), and the first derivative of XANES spectra (d). The Mössbauer measurement was performed at room temperature and calibrated *vs.* α-Fe foil. The XAS spectra of FePc, FePcCl, and FeTPPCl were included as references.

Table 1 Mössbauer parameters and relative absorption area obtained for each component from the fitting of the experimental spectrum recorded at room temperature. The isomer shift is given *versus* that of α-Fe

	Relative area/%	Isomer shift/mm s^{-1}	Quadrupole splitting/mm s^{-1}	Linewidth/mm s^{-1}	Assignment	Ref.
Singlet	6.5	0.01	—	0.42	γ-Fe or superparam·Fe	5, 12, 17 and 31
D1	35.0	0.35	1.05	0.71	O_x–Fe^{III}–N_4 high spin	10 and 59
D2	58.5	0.35	2.71	1.22	Distorted Fe^{II}–N_4 intermediate spin	5, 12, 17 and 31

is the fingerprint of square-planar Fe^{2+}–N_4 moieties (D_{4h} symmetry).[14,16] While this feature is not perceptible in the XANES of the FePhenMOF–$ArNH_3$ catalyst (Fig. 3c), it does emerge in the first derivative of the XANES (Fig. 3d). The faintness of this feature appears to contradict the high relative area of D2 determined by Mössbauer (58.4% of the resonance area, Table 1) at first glance. It is noted that the line width (1.22 mm s^{-1}) of the D2 site in this catalyst lies in the range of that (1.1–1.4 mm s^{-1}) reported for the D2 in various pyrolyzed Fe–N–C materials,[5,31,52–54] but is much larger than that of bulk FePc (0.39 mm s^{-1}),[55] underlining the multiplicity of the local iron environments. This is not surprising as the D2 sites in the MOF-derived catalyst are hosted in highly disordered carbon matrix as shown above, which is drastically different from the carbon environment of the D2 sites in bulk FePc. This difference is further supported by the EXAFS data. The Fourier Transforms (FT) peaks between 2–3 Å present for the bulk FePc, which arise from the coherent scattering of the carbon atoms in the second shell (Fig. 3b), are absent for the FePhenMOF–$ArNH_3$ catalyst owing to the incoherent scattering from the disordered carbon. It is thus reasonable to infer that the square-planar Fe–N_4 structure is somewhat distorted when embedded in the disordered carbon matrix, which accounts for the weakness of the fingerprint feature as it is extremely sensitive to the local D_{4h} symmetry and will be greatly suppressed by the distortion.[51,56]

The *ex situ* FT-EXAFS data also show the presence of Fe–N_x and inorganic iron species (Fig. 3b) in FePhenMOF–$ArNH_3$. The low intensity of the Fe–Fe scattering peak at ~2.1 Å (without phase corrections) is indicative of the minimal amount of inorganic Fe species (Fig. 3b), in agreement with the low resonance area γ-Fe obtained by Mössbauer. Therefore, the *ex situ* Mössbauer and XAS data converge to the co-existence of multiple Fe–N_x moieties and minimal amount of inorganic Fe species in the catalyst.

However, profound discrepancies between *ex situ* Mössbauer and XAS results lie in the coordinates and oxidation state of the Fe–N_x species. The overall XANES profiles of the FePhenMOF–$ArNH_3$ dry powders are more analogous to those of iron(III) phthalocyanine chloride (FePcCl), iron(III) *meso*-tetraphenylporphine chloride (FeTPPCl) (Sigma-Aldrich) (Fig. 3c), and OH–Fe^{3+}–N_4 sites,[14,57] rather than those of the iron(II) phthalocyanine or porphyrins. In addition, the EXAFS fitting results further suggest that the average first shell coordinate number (CN) of the central Fe is greater than four (ESI,† Table S3). These *ex situ* XAS results together suggest that some of the D1 and/or D2 species in the dry powders are Fe^{3+}–N_4 moieties covered by oxygen adsorbates. These discrepancies also exist in the previous work reported by Zitolo *et al.*[5] They claimed that the O_2–Fe–N_4 with two different oxygen binding configurations are the active sites of the highly active MOF-derived Fe–N–C catalysts on the basis of *ex situ* XAS analysis, although their Mössbauer results point to the two Fe^{2+}–N_4 species (D1 and D2). It should be noted that the low-spin Fe^{2+}–N_4 moiety (D1) cannot be distinguished from the high-spin Fe^{3+}–N_4 moiety only on the basis of Mössbauer analysis due to their comparable Mössbauer parameters such as isomer shift and quadrupole splitting.[58] Some researchers indeed assigned D1 to a six-coordinate Fe^{3+} compound.[10,59] However, such an assignment encounters another problem that the six-coordinate Fe^{3+} compound is coordination saturated and not accessible by oxygen molecules. The affinity of O_2 for six-coordinate Fe^{3+} compound has not yet been reported.[55]

2.4 *In situ* characterizations

These difficulties are well addressed by *in situ* XAS studies that characterize the local structure of active sites under operating conditions, hereby capturing structural and oxidation changes during ORR.[14] As shown in Fig. 4a, the Fe K-edge XANES of the FePhenMOF–$ArNH_3$ catalyst collected in O_2/N_2-saturated 0.1 M $HClO_4$ electrolyte shifts toward higher energy when the applied potential is increased from 0.1 to 1.0 V. These XAS spectra as a function of applied potential are reversible. The concurrent increase in the intensity of the Fe–N/O scattering FT-EXAFS peak (Fig. 4b) is indicative of the adsorption of OH_{ads} as confirmed by the EXAFS fittings (ESI,† Table S3). The corresponding Δμ-XANES data (Fig. 4c) can be nicely reproduced by the theoretical Δμ-XANES obtained by subtracting the XANES of the bare FeN_4C_x model from that of the FeN_4C_x model with an axially bonded oxygen atom (Fig. 4d).[14,16] These XAS results, which have been previously observed on various Fe–N–C catalysts,[14] point to the Fe^{2+}–N_4/O_x–Fe^{3+}–N_4 redox transition associated with the oxygen species adsorption. The oxygen adsorbates come exclusively from water activation in the N_2-saturated 0.1 M $HClO_4$ electrolyte (eqn (1)), and/or ORR (eqn (2)) in the O_2-saturated 0.1 M $HClO_4$ electrolyte. The identical *in situ* XAS signals obtained in O_2/N_2-saturated electrolytes indicate that the Fe^{2+}–N_4/OH_{ads}–Fe^{3+}–N_4 transition is controlled by the redox potential of the site in aqueous conditions.

$$Fe^{2+}\text{–}N_4 + H_2O \leftrightarrow OH_{ads}\text{–}Fe^{3+}\text{–}N_4 + H^+ + e^- \quad (1)$$

$$Fe^{2+}\text{–}N_4 + 1/2O_2 + H^+ + e^- \rightarrow OH_{ads}\text{–}Fe^{3+}\text{–}N_4 \quad (2)$$

Significantly, the *ex situ* XANES, FT-EXAFS, and Δμ-XANES data of the FePhenMOF–$ArNH_3$ dry powders nearly overlap those of

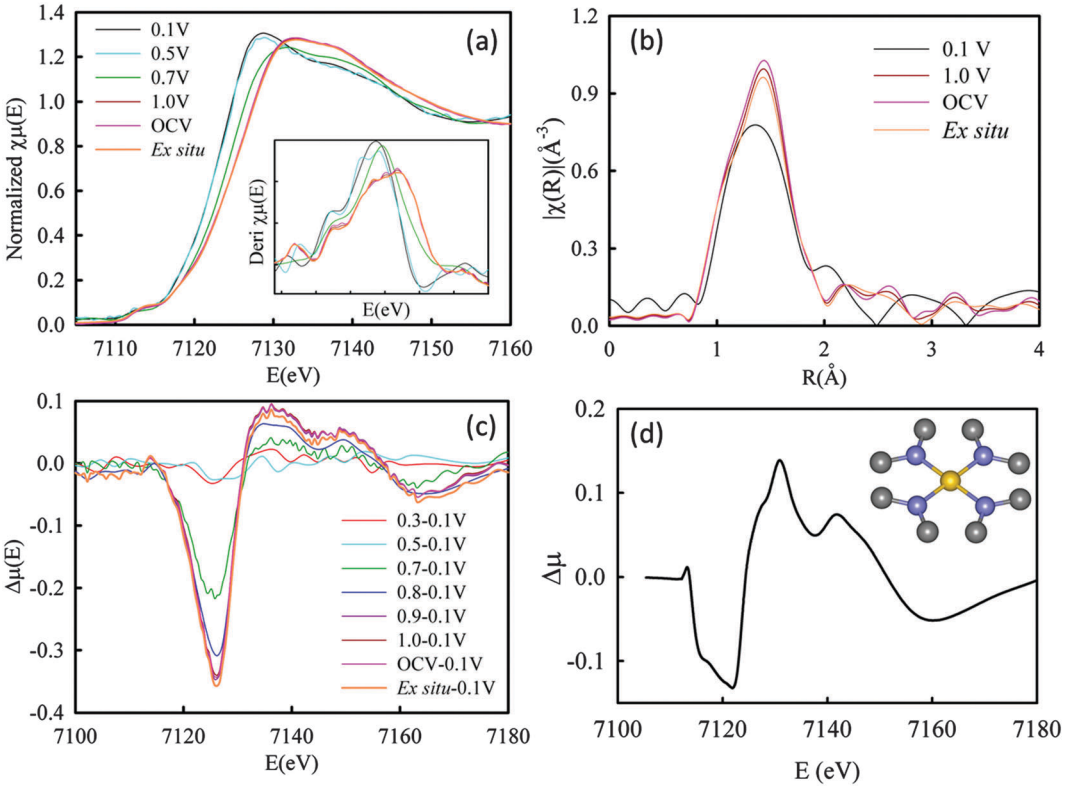

Fig. 4 *Ex situ* and *in situ* XANES (a), FT-EXAFS (b), and $\Delta\mu$-XANES (c) of the FePhenMOF–$ArNH_3$ catalyst. *Ex situ* data were firstly collected on the dry electrode, and the *in situ* spectra were collected at 0.1–1.0 V on the same electrode in O_2/N_2-saturated 0.1 M $HClO_4$ at room temperature; not all *in situ* data are displayed in (a) for simplicity, and the figure with full dataset is provided in ESI,† Fig. S4; and (d) theoretical $\Delta\mu$-XANES obtained by FEF9 calculations using the structural model (Fe–N_4–C_8) (inset) with/without axially bound O atom. The Fe, N, C, and O atoms are represented by yellow, blue, grey, and red spheres, respectively.

the *in situ* electrode at potentials above the redox potential such as 1.0 V or the open circuit voltage (OCV = 0.98 V) (Fig. 4). This provides unequivocal evidence that the exposed active sites in FePhenMOF–$ArNH_3$ at *ex situ* aerobic conditions are in the form of Fe^{3+}–N_4 moieties covered by oxygen adsorbates (coming from the air) as under elevated potentials, rather than the reduced Fe^{2+}–N_4 moieties at low potentials. These results are in direct contrast with the absence of ferric Fe signal in electron paramagnetic resonance (EPR) for Fe–N–C catalysts that solely contain FeN_xC_y moieties (*i.e.* showing only doublets D1 and D2 in Mössbauer spectroscopy).[31] However, the *ex situ* XANES of their Fe–N–C samples with poorly defined XANES features are similar to that of the ferric FeTMPPCl/C or to that of our FePhenMOF–$ArNH_3$ dry powders, but drastically different from that of ferrous FePc/C (Fig. 4 in ref. 31) with well-defined XANES features.[31] Although no explanation for the discrepancies can be proposed at this time, it is worth noting that their Fe–N–C sample was subjected to intense deoxygenation pre-treatment before the EPR measurements that were conducted at 5 K,[31] whereas the *ex situ* electrodes for the XAS measurements here had been exposed to air at room temperature without any pre-treatments. Considering the comparable Mössbauer parameters between zero-spin Fe^{2+}–N_4 and high-spin Fe^{3+}–N_4 moieties, the D1 site is assigned to the high-spin O_x–Fe^{3+}–N_4 rather than low-spin Fe^{2+}–N_4 moiety here. This assignment is strongly supported by the fact that the IS and QS values of D1 are close to those (IS = 0.18 mm s^{-1}; QS = 1.00 mm s^{-1}) of the μ-oxo derivative of FePc with the local configuration of high-spin Fe^{3+} coordinated by four equatorial nitrogen atoms and one axial oxygen atom.[55] This assignment attractively solves the discrepancies between *ex situ* Mössbauer and *in situ* XAS results. The coordinate saturation difficulty is naturally resolved because the active sites during ORR are not the Fe^{3+}–N_4 moieties covered by oxygen adsorbates identified at *ex situ* conditions or *in situ* at potentials higher than the $Fe^{2+/3+}$ redox potential, but the counterpart Fe^{2+}–N_4 moieties below the Fe^{2+}/Fe^{3+} redox potential for pyrolyzed moieties.

In addition to the Fe oxidation state and coordinates, the bulk average Fe–N bond distance (R_{Fe-N}) also changes drastically upon the Fe^{2+}/Fe^{3+} redox transition, which is however not manifested in eqn (1) and (2). The R_{Fe-N} obtained at 1.0 V or dry powders (1.99 Å) agrees well with those of analogous MOF-derived Fe–N–C catalysts given by combined EXAFS and XANES analysis (1.99–2.01 Å).[5] This R_{Fe-N} is identical to that of iron porphyrins (1.99–2.01 Å) and the analogous MOF-derived Fe–N–C catalysts,[5] suggesting the in-plane Fe configuration for both D1 and D2 sites corroborated by *ex situ* Mössbauer results. On the other hand, the R_{Fe-N} obtained at 0.1 V (2.07 Å) is much longer, which strongly indicates the presence of ferrous FeN_xC_y moieties with out-of-the-plane Fe configuration. This is further

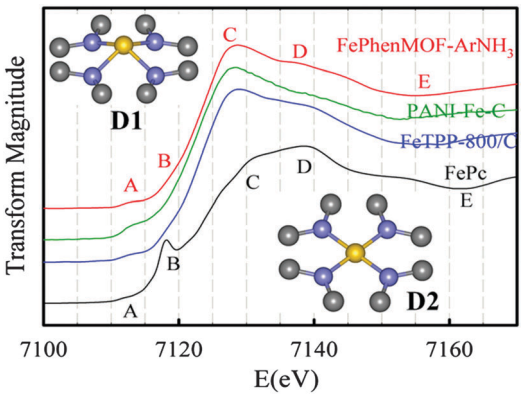

Fig. 5 XANES spectra of FePhenMOF–$ArNH_3$ collected at 0.1 V in N_2-saturated 0.1 M $HClO_4$; the XANES spectra of bulk FePc as a square-planar Fe^{2+}–N_4 standard is included as a reference of D2 (inset). XANES spectra of PANI–Fe–C and FeTPP-800/C collected at the same conditions (reproduced from our earlier work[14]) are also included for comparison. Note the differences in the relative intensity of features C and D.

confirmed by XANES spectra that are ultrasensitive probes of the electronic configuration and local geometry of the probed atoms.[14] As seen in Fig. 5, FePc and FePhenMOF–$ArNH_3$ exhibit the features A–E with different amplitude and/or position, which are diagnostic of the local structure differences within the Fe^{2+} complexes with varied Fe–N bond distances or local symmetry.[14] While the features A–E of FePc are the fingerprints of the square-planar Fe–N_4 structure, the features A–E of FePhenMOF–$ArNH_3$ (MOF-derived), FeTPP-800/C (macrocycle-derived), and PANI–Fe–C (polymer-derived) catalysts[14] are fairly similar, and represent an non-planar Fe–N_4 structure (a detailed discussion regarding the XANES analysis can be found in our previous publication)[14] (Fig. 5). These *in situ* XANES results are in agreement with the recent findings that almost all the pyrolyzed Fe–N–C catalysts contains both D1 and D2 sites irrespective of the precursor materials.[5,17,18] Given the in-plane Fe configuration of D2, D1 must have a distorted Fe–N_4 structure featured with out-of-plane Fe displacements and elongated Fe–N bond distances. The central Fe ion in D1 moves back toward the N_4-plane upon the adsorption of oxygen species, and the corresponding in-plane O_x–Fe–N_4 moiety is the site seen under *ex situ* conditions. This Fe–N switching behavior has been previously assigned to D3 with a fifth ligand X–Fe^{2+}–N_4 by us[14] on the basis of *in situ* XAS analysis, in addition to the fact that it is a typical Fe–N switching behavior for non-coplanar N_{axi}–Fe^{2+}–N_4 sites in biological macrocycles such as myoglobin.[60] However, the presence of D3 in FePhenMOF–$ArNH_3$ is not supported by Mössbauer. We therefore conclude that it is the D1 site that exhibits the unusual Fe–N switching behavior mimicking that of biological macrocycles despite the lack of the fifth ligand.

Compiling all the above results, D1 at low potential (below $Fe^{2+/3+}$ redox) is composed of a distorted Fe^{2+}–N_4 moiety embedded in amorphous carbon matrix characterized with out-of-plane Fe displacements. The central Fe ion moves back towards the plane upon the adsorption of oxygen species in the axial position at high potential (above $Fe^{2+/3+}$ redox) (Scheme 1).

These characteristic aspects of D1 are strikingly different from those of intact macrocycles such as FePc[61] or FeTPP:[14] a square-planar Fe^{2+}–N_4 moiety in ordered carbon environment with the central Fe shifting away from the N_4-plane upon oxygen species adsorption. These essential differences account for the superior ORR activity of the active site formed upon pyrolysis to that of the nonpyrolyzed Fe-macrocycle compounds. The poor ORR activity of D2 in acid is mainly attributed to the strong Fe–O binding energy that hinders oxygen adsorbate desorption,[62] as well as the completely filled d_{z^2} orbital of the intermediate-spin Fe that prevents the end-on adsorption of molecular oxygen.[18] Both of these detrimental factors are largely eliminated by the opposite Fe–N switching behavior of D1.[14] Specifically, the Fe–O binding energy of the in-plane O–Fe^{3+}–N_4 moiety is weaker than that of the out-of-plane O_x–Fe^{3+}–N_4 moiety; and the d_{z^2} orbital of the out-of-plane Fe^{2+}–N_4 motif is only partially filled.[14] This also supports the previous report by Kramm *et al.*[12] that attributed the higher TOF of D1 to the higher electron density of the central Fe, as the longer Fe–N bond distance of D1 decreases the Fe-to-ligand back-donation resulting in an increase of the electronic charge at the Fe center.[63] The weakening of the Fe–O binding energy, or the enrichment of the electron density is expected to increase the $Fe^{2+/3+}$ redox potential. Indeed, the $Fe^{2+/3+}$ redox potential of the D1 in FePhenMOF–$ArNH_3$ (0.78 V) is higher than that of the D2 in bulk FePc (0.64 V) (ESI,† Fig. S5).[24] If assuming the local structures of the D2 in FePhenMOF–$ArNH_3$ and in bulk FePc are not drastically different as supported by their similar Mössbauer parameters, the superior activity of D1 to that of D2 can be largely attributed to the higher redox potential, or equivalently the weaker Fe–O binding energy, that significantly alleviate the site-blocking effects according to the redox mechanism discussed below.

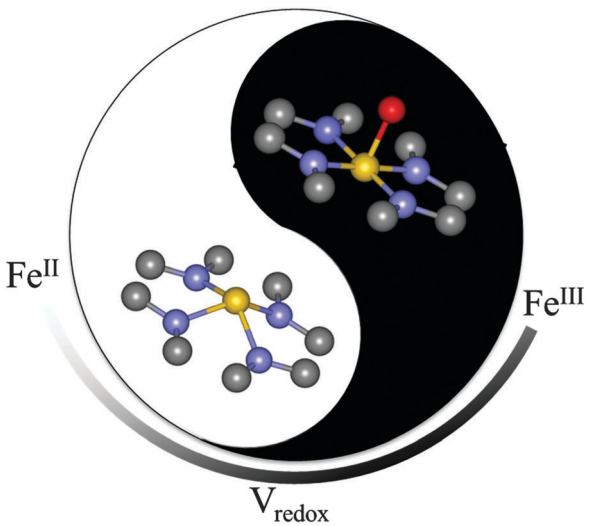

Scheme 1 The proposed local structure of D1, and the derived Fe–N switching behavior governed by the $Fe^{2+/3+}$ redox potential is illustrated by the structural model (Fe–N_4–C_8) with/without axially bound O atom. The Fe, N, C, and O atoms are represented by yellow, blue, grey, and red spheres, respectively.

3. Discussions

Based on *in situ* XAS studies on macrocycle-derived and polymer-derived Fe–N–C catalysts, we recently proposed that the ORR process is mediated by the reversible $Fe^{2+/3+}$ redox transition that is driven by the potential difference between the redox potential and the applied potential, and the population of the catalytically active sites and the reaction rate can be expressed as:

$$N_{\text{active}} = N_{\text{total}} \frac{1}{1 + e^{\frac{F}{RT}(E - E_{\text{redox}})}} \quad (3)$$

$$\Theta_{O^*} = \frac{N_{\text{total}} - N_{\text{active}}}{N_{\text{total}}} = \frac{1}{1 + e^{-\frac{F}{RT}(E - E_{\text{redox}})}} \quad (4)$$

$$J \propto N_{\text{total}}(1 - \Theta_{O^*}) \exp\left(-\frac{\Delta H^*}{RT}\right) \exp\left(-\frac{E - E^0}{b}\right) \quad (5)$$

where J is the kinetics current density obtained at the applied potential E. N_{active} and N_{total} are the available and total number of surface active sites, respectively; F is the Faraday constant; R is the universal gas constant; T is the temperature; E_{redox} is the redox potential under the relevant operation conditions; Θ_{O^*} is the coverage by adsorbed oxygen species at potential E; ΔH^* is the activation entropy for the electrocatalytic process; E^0 is the standard potential for the Faradaic process; and b is the value of the Tafel slope.

The redox mechanism is also applicable to MOF-derived Fe–N–C catalysts. The $Fe^{2+/3+}$ redox behaviors (Fig. 4 or eqn (1) or (2)) of FePhenMOF–$ArNH_3$ under reactive conditions have been clearly observed by *in situ* XAS and RDE, and shown to be closely linked to the ORR onset (Fig. 2c). This is rationalized by *in situ* XAS results that the Fe^{3+}–N_4 moieties with the central Fe poisoned by oxygen adsorbates at elevated potentials are ORR inactive, and start to switch to catalytically active Fe^{2+}–N_4 sites once the applied potential approaches the Fe^{2+}/Fe^{3+} redox potential cathodically. The corresponding site-blocking effects as described by eqn (5) can be quantitatively evaluated using the surface sensitive $\Delta\mu$-XANES technique.[14] The increasing $\Delta\mu$ amplitude (denoted as $|\Delta\mu|$) with increasing potential up to 1.0 V (Fig. 4c) indicates that the Fe^{2+}–N_4 sites are progressively occupied by OH_{ads} until reaching occupancy saturation at 1.0 V. Thus the $|\Delta\mu_E|/|\Delta\mu_{1.0V}|$ represents the relative OH_{ads} coverage (Θ_{O^*}) at a potential E. As seen in Fig. 6, the Θ_{O^*} quickly decrease with decreasing potentials from 0.9 to 0.6 V (black), highlighting the dominant role of site-blocking effects in the ORR kinetic region. The Θ_{O^*} has the same onset as that of the theoretical Θ_{O^*} derived from eqn (4) using the experimental $Fe^{2+/3+}$ redox potential of D1 (0.78 V) (Fig. 6), but the overall shape is more spread-out. This generally means that more than one species undergo the redox transition within the ORR kinetic region.[14,64] Indeed, the $Fe^{2+/3+}$ redox transition of D2 is supported by the gradual drop of the shoulder at 7117 eV (fingerprint of the square-planar Fe–N_4) in the first derivative of XANES with increasing potentials (the inset in Fig. 4a). The similar phenomenon has been observed on various original Fe–N_4 macrocycles including FePc/C,[61] FeTMPP/C,[64] and those pyrolyzed at low temperature without decomposing the square-planar Fe–N_4 configuration such as FePc-300/C (FePc pyrolyzed at 300 °C, ESI,† Fig. S6) and FeTPP-300/C.[14,16] Furthermore, the theoretical Θ_{O^*} (green dashed curve) calculated by using the relative content of both D1 and D2 derived from the relative areas given by Mössbauer (Table 1) closely matches the experimental Θ_{O^*} (black dots). This provides strong evidence that both D1 and D2 are directly involved into the ORR, but with different contributions to the measured activity discussed below.

A comprehensive understanding of the ORR activity of Fe–N–C catalysts can be gained from eqn (5). First, a highly active Fe–N–C catalyst shall have abundant catalytically active sites (D1) accessible by reactant molecules as reflected by the first term N_{total}. This requires high micropore surface area as they are closely related to active site population.[8,17] In addition, only a fraction of the active sites in many Fe–N–C catalysts are accessible by O_2, and thus the utilization of the active sites also contributes to N_{total}.[40] These understandings highlight the necessity of multiple pyrolysis applied here and elsewhere,[5–8] as it greatly increases the S_a and BET area shown above, hereby improving the utilization of the active sites as recently demonstrated by Sahraie *et al.*[40] Moreover, our decoration synthesis method that forms active sites preferentially in the surface regions can also increase the utilization of the active sites. This compensates the relatively low Fe content of the catalyst (0.5 wt%) and makes important contributions to the high activity of the catalyst.

The site-blocking effect is represented in the pre-exponential factor $(1 - \Theta_{O^*})$. It indicates that the activity is proportional to the unoccupied active sites at the target potential. Since the Θ_{O^*} as a function of E exhibits a sharp slope centered at the

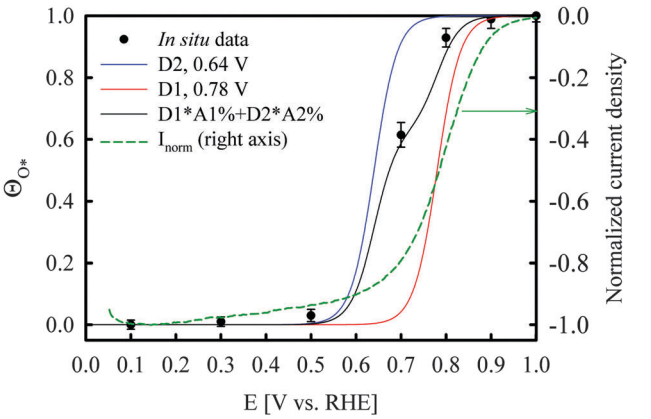

Fig. 6 The experimental Θ_{O^*} (black) as a function of potential for the FePhenMOF–$ArNH_3$ catalyst, in comparison to the calculated $\Theta_{O^*}(s)$ derived from eqn (4) using the redox potential of 0.78 V for D1 (red) and 0.64 V for D2 (blue), respectively. In addition, the theoretical Θ_{O^*} calculated by using the relative content of D1 and D2 (A1% and A2%) derived from the relative areas given by Mössbauer (black line) is also included. The room temperature of 298 K is used for calculations. The vertical error bars refer to errors involved in determining Θ_{O^*} from multiple experimental scans collected at each potential. The normalized ORR current density derived from Fig. 2b is also presented (green dashed line).

E_{redox} (Fig. 6), the E_{redox} of a catalytically active site is not expected to be significantly lower than the target potential to ensure enough active sites are available for ORR. At the potential of 0.8 V, which is typically used for non-PGM catalyst activity evaluation, 99.8% of the electroactive D2 sites with a redox potential of 0.64 V are poisoned by oxygen adsorbates according to eqn (4); whereas only 70% of D1 sites with a redox potential of 0.78 V are poisoned. This provides the fundamental basis of the previous findings that D1 is responsible for the ORR activity of pyrolyzed Fe–N–C catalysts in acidic media, whereas D2 makes negligible contribution.[11,12,17] This is further supported by the observation that the normalized ORR current density derived from Fig. 2b correlates better with the theoretical Θ_{O^*} of D1 than that of D2 or the experimental Θ_{O^*} (Fig. 6). Therefore, the superior ORR activity of D1 to that of D2 can be largely attributed to the higher $Fe^{2+/3+}$ redox potential that significantly suppresses the site-blocking effects.

In addition to D1 and D2 sites, N_xC_y sites are also presented in the catalyst as supported by the abundant pyridinic nitrogen (Fig. 1g). Given that activities reported for the sites were far inferior to those of Fe–N–C catalysts in acid,[20,29,30,32,65] their contributions to the measured ORR activity of FePhenMOF–$ArNH_3$ is negligible. This is directly supported by Dodelet *et al.*'s recent work showing that the similar MOF material exhibits an onset potential of ~0.8 V in acid, which is more than 150 mV lower than that of the counterpart MOF-derived Fe–N–C catalyst.[29]

Lastly, the kinetic effect lies in the exponential factor $\exp\left(-\frac{\Delta H^*}{RT}\right)$, which determines the intrinsic activity, or the turn-over frequency (TOF) of the FeN_xC_y center. It is noted that the TOF and E_{redox} are strongly coupled to each other as both are largely determined by the intrinsic property of the active site. While a high E_{redox} can effectively eliminate the site-blocking effect, the corresponding overly weak metal–oxygen binding energy may lead to low TOF such as the cobalt phthalocyanine with a redox potential of ~1.0 V in the pH = 1 solution.[62,66] By taking both TOF and E_{redox} factors into considerations, it is suggested that the optimal E_{redox} is in the range of 300–400 mV lower than the E^0 of the ORR (1.23 V).[67,68] The high TOF of the D1 site in our catalyst is therefore justified by the $Fe^{2+/3+}$ redox potential (~0.78 V) approaching this region. Indeed, the TOF of the D1 site at 0.8 V calculated following the protocol in the recent work[31] is 2.40 e s^{-1} $sites^{-1}$, which is ~40 times higher than the TOF of the Fe–N–C catalyst reported in that work, and about eight times higher than that of the Fe–N–C catalyst reported by Zitolo *et al.*[5] (details for the calculations of TOF and site density and the comparisons are given in the ESI† and Table S5).

It is noted that the TOFs are evaluated based on the total D1 content estimated by Mössbauer. However, Sahraie *et al.*[40] recently showed that only a fraction of D1 sites contribute to the measured activity of Fe–N–C catalysts because not all the D1 sites are accessible by O_2 by using polyaniline-derived Fe–N–C materials as model systems. In addition, a large fraction of the O_2-accessible D1 sites are poisoned by oxygen adsorbates at 0.8 V (Fig. 6). Therefore, the TOFs estimated by this method are much lower than the intrinsic TOFs. The TOF of the polyaniline-derived Fe(Mn)–N–C catalysts (~1.5 e s^{-1} $sites^{-1}$) obtained by considering the active site utilization determined by CO pulse chemisorption[40] is much higher than the corresponding TOF obtained following the method used here without considering the active site utilization (~0.93 e s^{-1} $sites^{-1}$), but still lower than ours. The only TOF value that exceeds ours was reported by Dodelet's group[18] on the D3 site: (N–FeN_{2+2}···NH^+/C: TOF (0.8 V) ≈ 10 e s^{-1} $sites^{-1}$). However, they recently abandoned this site on the basis of new experimental results.[29] Despite the lack of a rigorous evaluation of the TOF of Fe–N–C sites today, the high TOF of the D1 site in FePhenMOF–$ArNH_3$ is sufficiently confirmed by the comparisons, as well as the high ORR activity demonstrated in both RDE and PEMFCs with low Fe loading (~0.5 wt%). The high TOF is attributable to the high utilization of D1, and more importantly the nearly optimized $Fe^{2+/3+}$ redox potential that balances the site-blocking effects and O_2 dissociation.

Overall, the high ORR activity of the FePhenMOF–$ArNH_3$ catalyst is ascribed to the combination of the abundance of the reactant-accessible D1 sites with high TOF and near-optimal $Fe^{2+/3+}$ redox potential as manifested by eqn (5). The elucidation of the factors that make important contributions to the overall catalytic activity may pave the way to the rational design of non-PGM catalysts.

4. Conclusions

In this work, we have reported a MOF-derived Fe–N–C catalyst synthesized *via* a facile and scalable route and demonstrate its exceptional ORR activity in both R(R)DE and practical H_2/air PEMFCs. The non-planar ferrous $Fe–N_4$ moiety embedded in disordered carbon matrix has been identified as the active site (D1) responsible for the high ORR activity. This site reversibly switches to an in-plane ferric $Fe–N_4$ moiety covered by oxygen adsorbates when the applied potential crosses the $Fe^{2+/3+}$ redox potential anodically, with the population of the available active sites controlled by the redox potential. The biomimetic dynamic nature of this site is opposite to that of the intact square-planar ferrous $Fe–N_4$ moiety (D2) in original macrocycles. This key difference in dynamic nature between the D1 and D2 sites accounts for the weakened Fe–O binding energy and higher $Fe^{2+/3+}$ redox potential of D1 sites, and responsible for the superior intrinsic activity of D1 to that of D2. These results, in combination with our previous studies on macrocycle-derived and polymer-derived Fe–N–C catalysts, has demonstrated that the FeN_xC_y moieties (D1 and/or D2) mediate the ORR *via* the redox electrocatalytic process with potential-dependent population of active sites, with the intrinsic activity governed by the redox potential. On the basis of these findings, the exceptional ORR activity of the FePhenMOF–$ArNH_3$ catalyst can be largely ascribed to the highly porous and disordered carbon matrix environment that embrace (1) the favorable local environment anchoring distorted D1 sites with high TOF; (2) the

high density of reactant-accessible D1 sites; and (3) efficient mass transportation of ORR-related species.

5. Experimental

5.1 Catalyst preparation

Zinc oxide was heat treated at 400 °C in air prior to use. 0.81 g zinc oxide, 1.64 g 2-methylimidazole, and 0.053 g ammonia sulfate were ball milled for one hour in the presence of 10 μL methanol. The addition of a small amount of a liquid phase during reactive ball milling synthesis is to improve the reaction rate by enhancing the mobility and avoiding the limitations related to solubility. The reaction between ZnO and the ligand forming ZIF-8 structure is promoted by salt additive $(NH_4)_2SO_4$ through the protonation of 2-methylimidazole.[69] 75 mL polypropylene grinding vial and two 3/8 inch methacrylate balls were used as the container and the grinding media, respectively. Then 0.0435 g iron(II) acetate and 3.60 g 1,10-phenanthroline monohydrate were added and ball milled for two hours. The excess amount of Phenanthroline is required to give the best ORR performance for lab-scale catalysts, probably to prevent the exchange of metal ions between ZIF-8 and the Fe complex. The resulting light pink solid, FePhenMOF, was subjected to a first heat-treatment in argon at 1050 °C for one hour (denoted as FePhenMOF–Ar) with a ramping rate of 15 °C min^{-1} and then naturally cooled down to room temperature in the furnace with the heat off. A second heat treatment in ammonia was done at 1050 °C for 18 minutes (denoted as FePhenMOF–ArNH_3) with a ramping rate of 15 °C min^{-1} and then cooled down the same way as the Ar heat treatment. Ar/NH_3 was flowed into the tube furnace half an hour before applying any heat till the furnace cooled down to room temperature, and 1.3–1.5 gram catalysts was obtained after these two heat treatments with a yield of 22–25%. The catalyst was subjected to acid leaching in 0.1 M HCl at 80 °C overnight (>12 hours) with continuous stirring. The Fe loading in the FePhenMOF–ArNH_3 catalyst is 0.77 wt% before acid wash and 0.5 wt% after acid wash as confirmed by inductively coupled plasma mass spectrometry (ICP-MS).

5.2 Electrochemical measurements

Catalysts inks were prepared by dispersing 3.1 mg catalyst in a volume of 1 : 3 millipore water:isopropyl alcohol with 1 vol% of 5 wt% Nafion® as a binder. The ink solution was then sonicated approximately 60 minutes. 30 μL of the ink was pipetted on the glassy carbon disk to reach a loading of 600 μg cm^{-2}. All electrochemical measurements were carried out at room temperature in a standard electrochemical cell (Chemglass) using a rotating ring disk electrode (R(R)DE) setup from Pine Instrument Company connected to an Autolab bipotentiostat (PGSTAT302N). Cyclic voltammetry was run in 0.1 M perchloric acid ($HClO_4$) bubbled with argon. ORR measurements was carried out in the same electrolyte solution bubbled with pure oxygen gas with rotations at 400, 625, 900, and 1600 rpm at a scan rate of 20 mV s^{-1}. All voltages reported were with respect to a reversible hydrogen electrode (RHE) made from the same solution as the electrolyte. The commercial Pt/C (46%) electrocatalyst used as a reference in this study is obtained from Tanaka Kikinzoku International KK (Japan). Square-wave voltammetry (SWV) experiments were performed using a step potential of 5 mV, potential amplitude of 20 mV, and scan frequency of 10 Hz. Catalyst mass activity (I_m) in units of A g^{-1} was calculated according to $I_m = I_{kin}/L_{catalyst}$, where $L_{catalyst}$ is the geometric catalyst loading ($mg_{catalyst}$ cm^{-2}_{geo}) and I_{kin} is the geometric kinetic current density, which was estimated according to: $I_{kin,0.8V} = I_{0.8V} \times I_{lim}/(I_{lim} - I_{0.8V})$, using the geometric current density at 0.8 V *versus* RHE, $I_{0.8}$, and the diffusion limited current density, I_{lim}.

5.3 PEMFC measurements

Membrane Electrode Assemblies (MEAs, 5 cm^2) for fuel cell testing were prepared from Gas Diffusion Electrodes (GDE) pressed onto 211 Nafion® membrane with PTFE-impregnated glass-fiber sub-gaskets at 131 °C for 10 minutes under 450 psi, then allowed to cool under 1 psi pressure. The gas diffusion electrode were sprayed using Sono-tek Exacta-Coat automated spray system delivering 2 mL min^{-1} ink through a 25 kHz ultrasonic nozzle onto SGL 25BC Gas Diffusion Layer (GDL) materials heated to 65 °C. Cathode ink was deposited in a rate of 40 μg cm^{-2} per deposition pass, for a total of 2 $mg_{catalyst}$ cm^{-2}. The ink was composed of 4 mL Isopropyl Alcohol, 2 mL deionized water, 200 mg of catalyst mixed, 300 mg D2021 Nafion® dispersion. A 50 mL vessel containing the ink ingredients was placed in a water bath and mixed for 30 minutes using an IKA T-18 high shear mixer with S18-19G dispersing element set for 18 000 rpm. Anode was similarly prepared using JM Hispec 2000 catalyst (10 wt% Pt/C) with 30 wt% Nafion used and 1 mg cm^{-2} of Pt/C deposited on 25BC for total precious metal loading for 0.1 mg_{Pt} cm^{-2}. The MEAs were loaded into the cell testing assembly using single serpentine pattern graphite flow plates and the cell hardware was assembled using 4.5 N torque. The fuel cell was operated at 80 °C under a feed 200 sccm of 90% RH air and H_2 and 2 bar back pressure.

5.4 Physicochemical characterizations

X-ray diffraction (XRD) was performed on a Rigaku (model Ultima-IV) diffractometer with Cu Kα radiation (λ = 1.5418 Å) at 40 kV and 44 mA. The count time was 1.5 s and the step width was 0.1°. N_2 adsorption analysis was performed on a Quantachrome NOVA 2200e at 77 K. Total surface area was determined by the Brunauer–Emmett–Teller (BET) method, and pore size distribution was determined using Non-Local Density Functional Theory (NLDFT) split pore method from the NovaWin software. Particle morphology and chemical composition were performed on a Hitachi S-4800 field emission scanning electron microscope (SEM) with an accelerating voltage of 3–5 keV. Samples were mounted on a carbon-free adhesive stub attached to an aluminum sample stage. For transmission electron microscope (TEM), Karaa JEOL 2010 field emission gun TEM was used at an acceleration voltage of 200 kV with samples deposited on a holey carbon film on a 300 mesh copper grid. Raman spectra were collected using a DXRxi Raman microscope. X-ray photoelectron spectroscopy (XPS) spectra were acquired

on a Kratos Axis Ultra DLD X-ray photoelectron spectrometer using an Al Kα source monochromatic operating at 150 W. Acquisition times were 4 min for survey spectra, 3 min for C 1s s spectra, and 7 min for N 1s spectra. Data analysis and quantification were performed using XPSpeak41 software. The weight percentages of Fe in FePhenMOF–$ArNH_3$ catalyst before and after acid wash were quantified using ICP-MS.

5.5 X-Ray absorption spectroscopic (XAS) measurements

The *ex situ* and *in situ* XAS studies were performed at the 10-ID beamline (MRCAT) of the Advanced Photon Source (APS, Argonne National Laboratory, IL), and the X3B beamline National Synchrotron Light Source (Brookhaven National Laboratory). A detailed description of the *in situ* spectro-electrochemical cell design is given elsewhere.[70] Spectra at Fe K-edge were collected in fluorescence mode using a 32-elements GE solid state dectector (X3B) or a pips detector (10-ID). Measurements were performed at different electrode potentials from 0.1 V to 1.0 V *vs.* RHE (all the potentials mentioned in this paper are *versus* RHE unless otherwise specified). Details of electrochemical procedure associated with the *in situ* XAS measurements, and the XAS data analysis are described in our previous work,[71–73] and also provided in the ESI.†

5.6 ^{57}Fe Mössbauer spectroscopy measurements

The *ex situ* Mössbauer spectroscopy studies were performed at ICGM-AIME (Montpellier, France). ^{57}Fe Mössbauer spectra were measured with a ^{57}Co:Rh source. The measurements were performed keeping the source and absorber at room temperature. The spectrometer was operated with a triangular velocity waveform, and a gas filled proportional counter was used for the detection of the γ rays. Velocity calibration was performed with an α-Fe foil. The spectrum was fitted with appropriate combinations of Lorentzian lines. In this way, spectral parameters such as the isomer shift (IS), the electric quadrupole splitting (QS), the linewidth at half maximum (LW), the hyperfine fields (*H*) and the relative resonance areas (*A*) of the different components were determined. All values of the isomer shift are reported relative to α-Fe at room temperature.

Conflict of interest

The authors declare no competing financial interests.

Author contributions

J. L. and S. M. conceived and synthesized the FePhenMOF–$ArNH_3$ catalyst. J. L., S. G., S. M., and Q. J. conceived and designed the XAS and RDE experiments. J. L. and Q. J. conducted the XRD and Raman experiments. W. L. carried out the SEM and TEM experiments. M. S. and F. J. performed the Mössbauer experiments and their interpretation. B. H., S. M., and G. M. conducted H_2/air fuel cell testing and the scale-up of the FePhenMOF–$ArNH_3$ catalyst. C. M., X. Y., and Z. M. conducted the XPS experiments and their interpretation. J. L., F. J., Z. M., S. M., and Q. J. aggregated the figures and co-wrote the manuscript. All authors discussed the results, drew conclusions and commented on the manuscript.

Acknowledgements

The authors deeply appreciate financial assistance from the U.S. Department of Energy, EERE (DE-EE-0000459). Use of the National Synchrotron Light Source (beamline X3B), Brookhaven National Laboratory (BNL), was supported by the U.S. Department of Energy, Office of Basic Energy Sciences. This publication was made possible by the Center for Synchrotron Biosciences grant, P30-EB-009998, from the National Institute of Biomedical Imaging and Bioengineering (NBIB). Support from beamline personnel Dr Erik Farquhar and Mark Chance (X3B) are gratefully acknowledged. MRCAT operations are supported by the Department of Energy and the MRCAT member institutions. This research used resources of the Advanced Photon Source, a U.S. Department of Energy (DOE) Office of Science User Facility operated for the DOE Office of Science by Argonne National Laboratory under Contract No. DE-AC02-06CH11357.

References

1 H. A. Gasteiger, S. S. Kocha, B. Sompalli and F. T. Wagner, *Appl. Catal., B*, 2005, **56**, 9.
2 M. K. Debe, *Nature*, 2012, **486**, 43.
3 G. Wu, A. Santandreu, W. Kellogg, S. Gupta, O. Ogoke, H. Zhang, H.-L. Wang and L. Dai, *Nano Energy*, 2016, DOI: 10.1016/j.nanoen.2015.12.032.
4 M. Shao, Q. Chang, J.-P. Dodelet and R. Chenitz, *Chem. Rev.*, 2016, **116**, 3594.
5 A. Zitolo, V. Goellner, V. Armel, M.-T. Sougrati, T. Mineva, L. Stievano, E. Fonda and F. Jaouen, *Nat. Mater.*, 2015, **14**, 937.
6 K. Strickland, E. Miner, Q. Jia, U. Tylus, N. Ramaswamy, W. Liang, M.-T. Sougrati, F. Jaouen and S. Mukerjee, *Nat. Commun.*, 2015, **6**, 7343.
7 G. Wu, K. L. More, C. M. Johnston and P. Zelenay, *Science*, 2011, **332**, 443.
8 E. Proietti, F. Jaouen, M. Lefèvre, N. Larouche, J. Tian, J. Herranz and J.-P. Dodelet, *Nat. Commun.*, 2011, **2**, 416.
9 M. Lefèvre, E. Proietti, F. Jaouen and J.-P. Dodelet, *Science*, 2009, **324**, 71.
10 H. Schulenburg, S. Stankov, V. Schünemann, J. Radnik, I. Dorbandt, S. Fiechter, P. Bogdanoff and H. Tributsch, *J. Phys. Chem. B*, 2003, **107**, 9034.
11 U. I. Koslowski, I. Abs-Wurmbach, S. Fiechter and P. Bogdanoff, *J. Phys. Chem. C*, 2008, **112**, 15356.
12 U. I. Kramm, I. Abs-Wurmbach, I. Herrmann-Geppert, J. Radnik, S. Fiechter and P. Bogdanoff, *J. Electrochem. Soc.*, 2011, **158**, B69.
13 M. Ferrandon, A. J. Kropf, D. J. Myers, K. Artyushkova, U. Kramm, P. Bogdanoff, G. Wu, C. M. Johnston and P. Zelenay, *J. Phys. Chem. C*, 2012, **116**, 16001.
14 Q. Jia, N. Ramaswamy, H. Hafiz, U. Tylus, K. Strickland, G. Wu, B. Barbiellini, A. Bansil, E. F. Holby, P. Zelenay and S. Mukerjee, *ACS Nano*, 2015, **9**, 12496.

15 U. Tylus, Q. Jia, K. Strickland, N. Ramaswamy, A. Serov, P. Atanassov and S. Mukerjee, *J. Phys. Chem. C*, 2014, **118**, 8999.
16 N. Ramaswamy, U. Tylus, Q. Jia and S. Mukerjee, *J. Am. Chem. Soc.*, 2013, **135**, 15443.
17 U. I. Kramm, M. Lefèvre, N. Larouche, D. Schmeisser and J.-P. Dodelet, *J. Am. Chem. Soc.*, 2013, **136**, 978.
18 U. I. Kramm, J. Herranz, N. Larouche, T. M. Arruda, M. Lefevre, F. Jaouen, P. Bogdanoff, S. Fiechter, I. Abs-Wurmbach, S. Mukerjee and J.-P. Dodelet, *Phys. Chem. Chem. Phys.*, 2012, **14**, 11673.
19 A. L. Bouwkamp-Wijnoltz, W. Visscher, J. A. R. van Veen, E. Boellaard, A. M. van der Kraan and S. C. Tang, *J. Phys. Chem. B*, 2002, **106**, 12993.
20 D. Guo, R. Shibuya, C. Akiba, S. Saji, T. Kondo and J. Nakamura, *Science*, 2016, **351**, 361.
21 B. Winther-Jensen, O. Winther-Jensen, M. Forsyth and D. R. MacFarlane, *Science*, 2008, **321**, 671.
22 Y. Hu, J. O. Jensen, W. Zhang, L. N. Cleemann, W. Xing, N. J. Bjerrum and Q. Li, *Angew. Chem., Int. Ed.*, 2014, **53**, 3675.
23 D. Deng, L. Yu, X. Chen, G. Wang, L. Jin, X. Pan, J. Deng, G. Sun and X. Bao, *Angew. Chem., Int. Ed.*, 2013, **52**, 371.
24 L. Birry, J. H. Zagal and J.-P. Dodelet, *Electrochem. Commun.*, 2010, **12**, 628.
25 C. A. Melendres, *J. Phys. Chem.*, 1980, **84**, 1936.
26 F. Calle-Vallejo, J. I. Martinez and J. Rossmeisl, *Phys. Chem. Chem. Phys.*, 2011, **13**, 15639.
27 S. Maldonado and K. J. Stevenson, *J. Phys. Chem. B*, 2004, **108**, 11375.
28 G. Liu, X. Li, P. Ganesan and B. N. Popov, *Electrochim. Acta*, 2010, **55**, 2853.
29 G. Zhang, R. Chenitz, M. Lefèvre, S. Sun and J.-P. Dodelet, *Nano Energy*, 2016, DOI: 10.1016/j.nanoen.2016.02.038.
30 J. Masa, W. Xia, M. Muhler and W. Schuhmann, *Angew. Chem., Int. Ed.*, 2015, **54**, 10102.
31 U. I. Kramm, I. Herrmann-Geppert, J. Behrends, K. Lips, S. Fiechter and P. Bogdanoff, *J. Am. Chem. Soc.*, 2016, **138**, 635.
32 J.-P. Dodelet, R. Chenitz, L. Yang and M. Lefèvre, *ChemCatChem*, 2014, **6**, 1866.
33 M. Tavakkoli, T. Kallio, O. Reynaud, A. G. Nasibulin, C. Johans, J. Sainio, H. Jiang, E. I. Kauppinen and K. Laasonen, *Angew. Chem., Int. Ed.*, 2015, **54**, 4535.
34 D. Y. Chung, S. W. Jun, G. Yoon, S. G. Kwon, D. Y. Shin, P. Seo, J. M. Yoo, H. Shin, Y.-H. Chung, H. Kim, B. S. Mun, K.-S. Lee, N.-S. Lee, S. J. Yoo, D.-H. Lim, K. Kang, Y.-E. Sung and T. Hyeon, *J. Am. Chem. Soc.*, 2015, **137**, 15478.
35 K. Artyushkova, A. Serov, S. Rojas-Carbonell and P. Atanassov, *J. Phys. Chem. C*, 2015, **119**, 25917.
36 T. S. Olson, S. Pylypenko, J. E. Fulghum and P. Atanassov, *J. Electrochem. Soc.*, 2010, **157**, B54.
37 E. F. Holby and C. D. Taylor, *Sci. Rep.*, 2015, **5**, 9286.
38 C. E. Szakacs, M. Lefevre, U. I. Kramm, J.-P. Dodelet and F. Vidal, *Phys. Chem. Chem. Phys.*, 2014, **16**, 13654.
39 S. Kattel and G. Wang, *J. Mater. Chem. A*, 2013, **1**, 10790.
40 N. R. Sahraie, U. I. Kramm, J. Steinberg, Y. Zhang, A. Thomas, T. Reier, J.-P. Paraknowitsch and P. Strasser, *Nat. Commun.*, 2015, **6**, 8618.
41 M. Dresselhaus, A. Jorio and R. Saito, *Annu. Rev. Condens. Matter Phys.*, 2010, **1**, 89.
42 H.-W. Liang, W. Wei, Z.-S. Wu, X. Feng and K. Müllen, *J. Am. Chem. Soc.*, 2013, **135**, 16002.
43 F. Jaouen, M. Lefèvre, J.-P. Dodelet and M. Cai, *J. Phys. Chem. B*, 2006, **110**, 5553.
44 F. Jaouen, J. Herranz, M. Lefevre, J.-P. Dodelet, U. I. Kramm, I. Herrmann, P. Bogdanoff, J. Maruyama, T. Nagaoka and A. Garsuch, *ACS Appl. Mater. Interfaces*, 2009, **1**, 1623.
45 P. H. Matter, E. Wang, M. Arias, E. J. Biddinger and U. S. Ozkan, *J. Mol. Catal. A: Chem.*, 2007, **264**, 73.
46 Y.-k. Zhou, B.-l. He, W.-j. Zhou, J. Huang, X.-h. Li, B. Wu and H.-l. Li, *Electrochim. Acta*, 2004, **49**, 257.
47 Q. Li, G. Wu, D. A. Cullen, K. L. More, N. H. Mack, H. T. Chung and P. Zelenay, *ACS Catal.*, 2014, **4**, 3193.
48 D. R. Rolison, *Science*, 2003, **299**, 1698.
49 J. Shui, C. Chen, L. Grabstanowicz, D. Zhao and D.-J. Liu, *Proc. Natl. Acad. Sci. U. S. A.*, 2015, **112**, 10629.
50 E. Kuzmann, A. Nath, V. Chechersky, S. Li, Y. Wei, X. Chen, J. Li, Z. Homonnay, M. Gál, V. K. Garg, Z. Klencsár and A. Vértes, *Hyperfine Interact.*, 2002, **139**, 631.
51 V. Briois, P. Sainctavit, G. J. Long and F. Grandjean, *Inorg. Chem.*, 2001, **40**, 912.
52 M. T. Sougrati, V. Goellner, A. K. Schuppert, L. Stievano and F. Jaouen, *Catal. Today*, 2016, **262**, 110.
53 C. H. Choi, C. Baldizzone, G. Polymeros, E. Pizzutilo, O. Kasian, A. K. Schuppert, N. Ranjbar Sahraie, M.-T. Sougrati, K. J. J. Mayrhofer and F. Jaouen, *ACS Catal.*, 2016, **6**, 3136.
54 U. I. Koslowski, I. Abs-Wurmbach, S. Fiechter and P. Bogdanoff, *J. Phys. Chem. C*, 2008, **112**, 15356.
55 A. A. Tanaka, C. Fierro, D. Scherson and E. B. Yaeger, *J. Phys. Chem.*, 1987, **91**, 3799.
56 M.-L. Boillot, J. Zarembowitch, J.-P. Itie, A. Polian, E. Bourdet and J. G. Haasnoot, *New J. Chem.*, 2002, **26**, 313.
57 R. Cao, R. Thapa, H. Kim, X. Xu, M. Gyu Kim, Q. Li, N. Park, M. Liu and J. Cho, *Nat. Commun.*, 2013, **4**, 2076.
58 F. Jaouen, *Non-Noble Metal Fuel Cell Catalysts*, Wiley-VCH Verlag GmbH & Co. KGaA, 2014, p. 29.
59 Y. Zhu, B. Zhang, X. Liu, D.-W. Wang and D. S. Su, *Angew. Chem., Int. Ed.*, 2014, **53**, 10673.
60 W. R. Scheidt and C. A. Reed, *Chem. Rev.*, 1981, **81**, 543.
61 I. C. Stefan, Y. Mo, S. Y. Ha, S. Kim and D. A. Scherson, *Inorg. Chem.*, 2003, **42**, 4316.
62 R. Chen, H. Li, D. Chu and G. Wang, *J. Phys. Chem. C*, 2009, **113**, 20689.
63 C. Fierro, A. B. Anderson and D. A. Scherson, *J. Phys. Chem.*, 1988, **92**, 6902.
64 I. T. Bae, D. A. Tryk and D. A. Scherson, *J. Phys. Chem. B*, 1998, **102**, 4114.
65 D. Singh, J. Tian, K. Mamtani, J. King, J. T. Miller and U. S. Ozkan, *J. Catal.*, 2014, **317**, 30.
66 A. van der Putten, A. Elzing, W. Visscher and E. Barendrecht, *J. Electroanal. Chem. Interfacial Electrochem.*, 1987, **221**, 95.
67 S. Gottesfeld, *ECS Trans.*, 2014, **61**, 1.

68 S. Gottesfeld, in *Fuel cell catalysis: a surface science approach*, ed. M. T. M. Koper, Wiley, Hoboken, NJ, 2009.
69 C. Mottillo, Y. Lu, M.-H. Pham, M. J. Cliffe, T.-O. Do and T. Friščić, *Green Chem.*, 2013, **15**, 2121.
70 T. M. Arruda, B. Shyam, J. S. Lawton, N. Ramaswamy, D. E. Budil, D. E. Ramaker and S. Mukerjee, *J. Phys. Chem. C*, 2010, **114**, 1028.
71 Q. Jia, K. Caldwell, J. M. Ziegelbauer, A. Kongkanand, F. T. Wagner, S. Mukerjee and D. E. Ramaker, *J. Electrochem. Soc.*, 2014, **161**, F1323.
72 Q. Jia, K. Caldwell, K. Strickland, J. M. Ziegelbauer, Z. Liu, Z. Yu, D. E. Ramaker and S. Mukerjee, *ACS Catal.*, 2014, **5**, 176.
73 Q. Jia, E. Lewis, C. Grice, E. Smotkin and C. Segre, *JPCS*, 2009, **190**, 012157.

